LETTER

doi:10.1038/nature17397

Measurement of the Earth tides with a MEMS gravimeter

R. P. Middlemiss[1,2], A. Samarelli[1], D. J. Paul[2], J. Hough[1], S. Rowan[1] & G. D. Hammond[1]

The ability to measure tiny variations in the local gravitational acceleration allows, besides other applications, the detection of hidden hydrocarbon reserves, magma build-up before volcanic eruptions, and subterranean tunnels. Several technologies are available that achieve the sensitivities required for such applications (tens of microgal per hertz[1/2]): free-fall gravimeters[1], spring-based gravimeters[2,3], superconducting gravimeters[4], and atom interferometers[5]. All of these devices can observe the Earth tides[6]: the elastic deformation of the Earth's crust as a result of tidal forces. This is a universally predictable gravitational signal that requires both high sensitivity and high stability over timescales of several days to measure. All present gravimeters, however, have limitations of high cost (more than 100,000 US dollars) and high mass (more than 8 kilograms). Here we present a microelectromechanical system (MEMS) device with a sensitivity of 40 microgal per hertz[1/2] only a few cubic centimetres in size. We use it to measure the Earth tides, revealing the long-term stability of our instrument compared to any other MEMS device. MEMS accelerometers—found in most smart phones[7]—can be mass-produced remarkably cheaply, but none are stable enough to be called a gravimeter. Our device has thus made the transition from accelerometer to gravimeter. The small size and low cost of this MEMS gravimeter suggests many applications in gravity mapping. For example, it could be mounted on a drone instead of low-flying aircraft for distributed land surveying and exploration, deployed to monitor volcanoes, or built into multi-pixel density-contrast imaging arrays.

Gravimeters can be split into two broad categories: absolute gravimeters and relative gravimeters. Absolute gravimeters measure the gravitational acceleration, g, by timing a mass in free fall over a set distance. Absolute gravimeters are very accurate but are bulky and expensive. The Micro-g Lacoste FG5 (ref. 1), for example, achieves acceleration sensitivities of $1.6\,\mu\mathrm{Gal\,Hz}^{-1/2}$ (that is, an acceleration measurement of $1.6\,\mu\mathrm{Gal}$ over an integration time of one second, where $1\,\mathrm{Gal} = 1\,\mathrm{cm\,s}^{-2}$), but it costs over \$US100,000 and weighs 150 kg. Relative gravimeters make gravity measurements relative to the extension of a spring: the deflection of a mass on a spring will change as g varies. These devices can be made smaller than absolute gravimeters but are intrinsically less stable: the spring constant can change with varying environmental conditions. The Scintrex CG5 relative gravimeter (also costing over \$US100,000, but weighing 8 kg) can measure gravity variations down to $2\,\mu\mathrm{Gal}$ (refs 2 and 3) but is much more susceptible to drift than absolute devices. For any mass-on-spring system, increased acceleration sensitivity is achieved by either improving the sensitivity to displacement, or by minimizing the ratio, k/m, between the spring constant, k, and the mass, m. A system in which a mass is suspended from a spring within a rigid housing will respond differently to signals above or below the resonant frequency. In the regime below the resonance there will be a linear relationship between the displacement of the proof mass and the acceleration of the housing. This is the region in which the device can be used as an accelerometer or gravimeter.

MEMS devices are microscopic mechanical devices made from semiconductor materials. They have the advantage of being mass-producible, light-weight and cheap. Although mobile phone accelerometers are not very sensitive, some MEMS devices have been developed that reach sensitivities much better than the $0.23\,\mathrm{mGal\,Hz}^{-1/2}$ of the iPhone MEMS device[7]. For example: a device developed by ref. 8 has a sensitivity of $17\,\mu\mathrm{Gal\,Hz}^{-1/2}$, the SERCEL QuietSieis[9] has a sensitivity of $15\,\mu\mathrm{Gal\,Hz}^{-1/2}$, and a microseismometer developed by ref. 10 has a sensitivity of $2\,\mu\mathrm{Gal\,Hz}^{-1/2}$. These devices, however, can only operate as seismometers and do not have sufficient stability to be classed as gravimeters, which are capable of monitoring low-frequency gravimetric signals such as the Earth tides (around $10\,\mu\mathrm{Hz}$). Extended Data Table 1 summarizes the characteristics of these MEMS seismometers, the Scintrex CG5 gravimeter, and our own gravimeter. Extended Data Fig. 7 provides a further comparison between our own device, the microseismometer in ref. 10, the Scintrex CG5 and two other commercial devices.

The Earth tides are an elastic deformation of the Earth's crust caused by the changing relative phases of the Sun, the Earth and the Moon[6]. They produce a small variation in the local gravitational acceleration, the size of which also depends on the latitude and elevation of the measurement location. Depending on the time of the lunar month, the Earth tides vary in amplitude and frequency, moving between diurnal ($2 \times 10^{-5}\,\mathrm{Hz}$) and semi-diurnal ($1 \times 10^{-5}\,\mathrm{Hz}$) peaks. Since the Earth tides have a peak signal strength[3] of less than $400\,\mu\mathrm{Gal}$, and a low-frequency oscillation, they are a useful natural signal with which to demonstrate both the sensitivity and long-term stability of any gravimeter.

Our device is designed to have a resonant frequency of under $4\,\mathrm{Hz}$. To achieve such low frequencies a geometric anti-spring system[11,12] was chosen. With increasing displacement, anti-springs get softer and their resonant frequency gets lower. A geometrical anti-spring requires a pair of arched flexures that meet at a constrained central point. In the case of our MEMS device they meet at the proof mass. This geometry constrains the motion of the proof mass to the axis shown in Fig. 1. As the proof mass is pulled away from its unloaded position the spring constant is lowered. This is in contrast to a spring obeying Hooke's law, in which the spring constant does not change with increasing displacement. Tilting the MEMS device from the horizontal to the vertical orientation pulls the proof mass down, thus lowering the frequency from over $20\,\mathrm{Hz}$ when horizontal to $2.3\,\mathrm{Hz}$ when vertical. We have opted for a configuration with a pair of anti-spring flexures supporting the lower portion of the proof mass, and a single flexure supporting the top. All of the flexures are only $5\,\mu\mathrm{m}$ wide but $200\,\mu\mathrm{m}$ deep. The three-flexure system maintains an anti-spring behaviour as the gravitational loading increases (when the device is tilted from horizontal to vertical). Owing to the asymmetry of the design, however, a small level of y-axis tilting occurs. This tilt pulls the system off its constrained axis. When the system reaches its equilibrium, it shows Hooke's law behaviour (see Methods and Extended Data Fig. 1 for further details). We thus
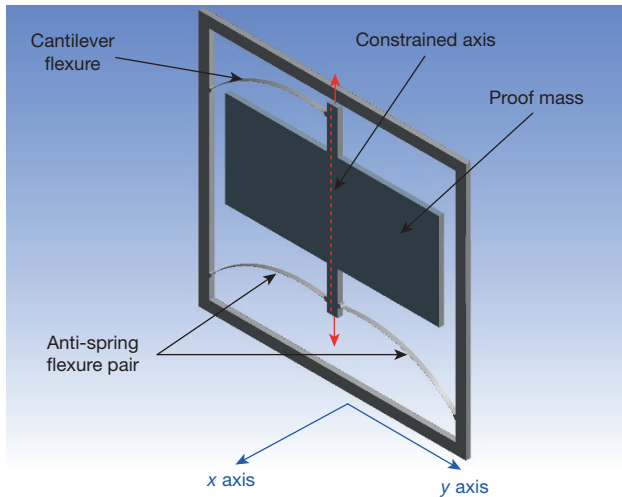
Figure 1 | The MEMS device. Design of the MEMS gravimeter. The central proof mass is suspended from three flexures: an anti-spring pair at the bottom and a curved cantilever at the top. The anti-spring pair constrains the motion of the proof mass along the constrained axis (red dashed line). The frequency is lowered by this constraint until the cantilever pushes the motion off-axis, stabilizing the MEMS device at a lower frequency.

have a device that is stable at a much lower frequency than traditional MEMS devices. A resonant frequency of 2.3 Hz is the lowest resonant frequency of any reported MEMS accelerometer so far. To our knowledge the next-lowest resonant frequency reported is 10.2 Hz in a device made by ref. 13. The fact that the system has Hooke's law behaviour in its vertical configuration means that it is less sensitive to tilt in the x axis (see Fig. 1) than would be the case for a normal geometrical anti-spring (see Extended Data Fig. 8).

The proof mass motion is measured using an optical shadow sensor[14]. Here a light-emitting diode (LED) illuminates a photodiode with the MEMS device mounted in between. Motion of the proof mass modulates the shadow, generating a change in the current output of the photodiode. This shadow sensor (Fig. 2) achieves a high sensitivity (equating to an acceleration noise floor of $\leq 10\,\mu$Gal at the sampling frequency of 0.03 Hz), while allowing a large dynamic range of up to 50 μm.

Observation of the Earth tides requires stable operation over several days. The main contributor to parasitic motion is the varying

temperatures of the system. For this reason the 'C'-shaped structure of the shadow sensor was fabricated from fused silica because of its low thermal expansion coefficient at room temperature ($4.1 \times 10^{-7}\,\mathrm{K}^{-1}$)[15]. Silicon has a much larger thermal expansion coefficient ($2.6 \times 10^{-6}\,\mathrm{K}^{-1}$)[16], but we used silicon to make the MEMS because it is a standard fabrication material in the semiconductor industry, it has high mechanical strength, and its thermal properties are well characterized. The dominant mechanism by which temperature variations affect the gravity measurement is the change in Young's modulus, Y, of the flexures[17,18]. This in turn alters the spring constant k of the flexures, giving $k^{-1}\mathrm{d}k/\mathrm{d}T = 7.88 \times 10^{-6}\,\mathrm{K}^{-1}$. We therefore implemented servo control loops to maintain the temperature of the system to within 1 mK. A change in temperature of 1 mK would give an uncertainty in the gravity reading of about 25 μGal. The primary control loop maintained the temperature of the MEMS device directly, the second controlling the temperature of a copper thermal shield that encased the entire shadow sensor (Fig. 2). The MEMS device was placed inside a vacuum system. This was bolted to the floor without an external seismic isolation table, which would be a large and expensive addition.

From December 2014 the system was left in continuous operation while the servo control was optimized. Figure 3 demonstrates a data run of five days between 13 and 18 March 2015 in which gravitational acceleration is plotted against time. The blue data demonstrates our experimental data averaged with a time constant of 240 min (the full noise data can be observed in Extended Data Fig. 2a), together with a data set filtered with a 10-min time constant (Extended Data Fig. 2b). The solid red line is a theoretical plot of the Earth tides as should be observed at our location (55.8719° N, 4.2875° W), and was plotted using *TSOFT*[19]. An ocean loading correction is also included in this theoretical plot to account for the effect of nearby tidal waters pressing on the Earth's crust, although the effect is at the level of 5% of the total signal for our laboratory. There is a strong correlation coefficient, R, of 0.86 between our experimental data and the theory plot, indicating that we have indeed measured the Earth tides with our MEMS device. This measurement provides a natural calibration for the gravimeter, the results of which allow us to determine that the present sensitivity of the device is $40\,\mu\mathrm{Gal\,Hz}^{-1/2}$. We further performed a stability test of the calibration factor for our device by monitoring the tides at two intervals approximately three months apart. The calibration remained constant to better than 5% (Extended Data Fig. 9).

The noise floor of our device is limited by seismic noise. A theoretical thermal noise floor of under $0.5\,\mu\mathrm{Gal\,Hz}^{-1/2}$ can be calculated, assuming that losses are due to structural damping[20]. This calculation is
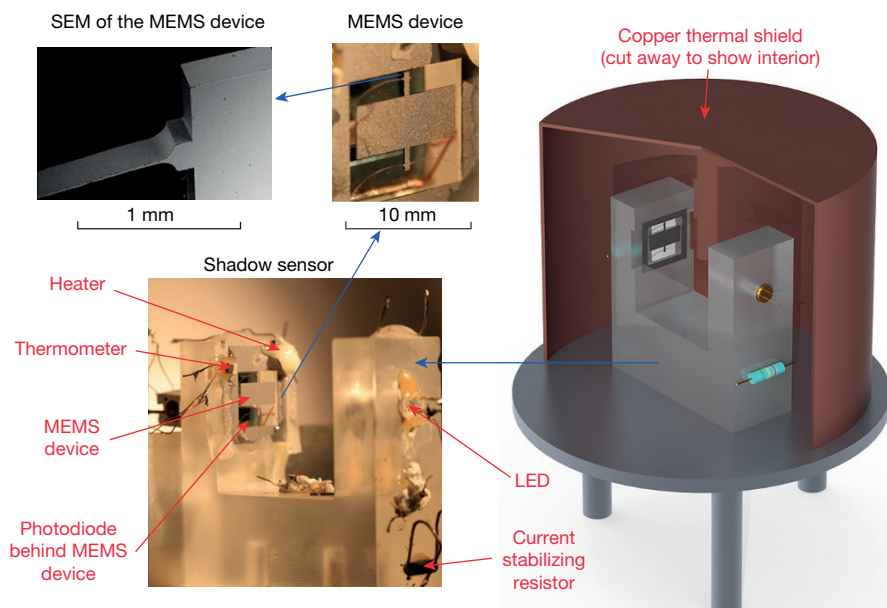
Figure 2 | The experimental set-up. The MEMS device and the shadow sensor. Both sit on an aluminium plate and are encased in a copper thermal shield. Both the MEMS device and the shield are thermally controlled. At the top left is a photograph and scanning electron microscope (SEM) image (copyright for both images R.P.M., 2015) of the MEMS device. At the bottom left is a photograph of the MEMS device mounted on the optical shadow sensor with glue holding the heater and thermometer in place (copyright G.D.H., 2015).
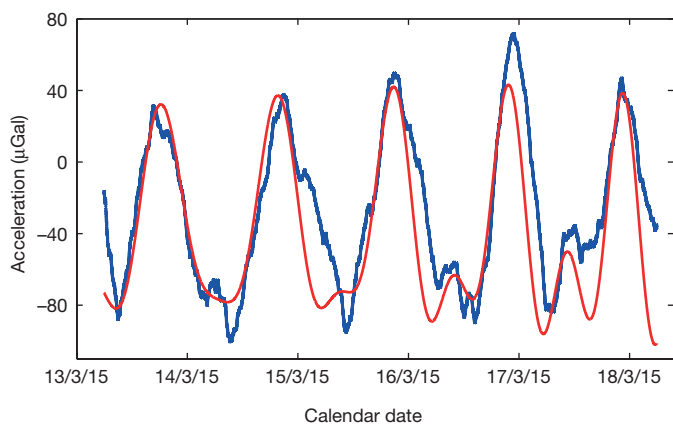
Figure 3 | The Earth tides. The measurements of the Earth tides obtained from the MEMS device. The data has been averaged with a time constant of 240 min. The red line is a theoretical plot calculated with *TSOFT*[19], including an ocean loading correction. The blue line is the experimental data. The two series have a correlation coefficient of 0.86.

based upon a measurement of the quality factor, Q, of the device under vacuum of about 80 (the relaxation time of the MEMS device is about 11 s). We observe that Q reduces as the resonant frequency is lowered

(Extended Data Fig. 3). This behaviour is observed in geometrical anti-springs because at low resonant frequencies the springs restoring force becomes comparable to internal friction[21].

To put the sensitivity of our device into context, $40\,\mu\text{Gal Hz}^{-1/2}$ is sufficient in 1 s to detect a tunnel with a cross-sectional area of $2\,\text{m}^2$ and length of 4 m at a depth of 2 m. It could be used to find oil reservoirs exceeding a size of $50\,\text{m} \times 50\,\text{m} \times 50\,\text{m}$ (with a density contrast of 50%) at a depth of 150 m. A change of $45\,\mu\text{Gal}$ was a 'clear precursor' to a volcanic eruption in the Canary Islands in 2011[22]. It is accepted that intrusion of new magma into a reservoir precedes volcanic eruptions[23] so continuous microgravity measurements around volcanoes are a useful tool in monitoring such events[24]. The ratio of ground deformation to change in gravity can be used to monitor magma chambers at depths of several kilometres[25].

In Fig. 3 a linear drift term has been removed from the data. This drift equates to less than $150\,\mu\text{Gal}$ per day, a factor of three better than the drift of the Scintrex CG5 ($500\,\mu\text{Gal}$ per day). Our MEMS device and the Scintrex CG5 auto-correct this drift with software. Figure 4 consists of eight subplots demonstrating the drift characteristics of the MEMS device. Figure 4a shows the full-noise tide data without a linear drift correction. Figure 4c shows the same data but with the tide signal removed. Figure 4e shows the same data again but with a linear drift correction. Figure 4g shows the same data as in Fig. 4e, but with a 240-min filter applied. Figure 4b, d, f and h shows the Allan deviation for the data in
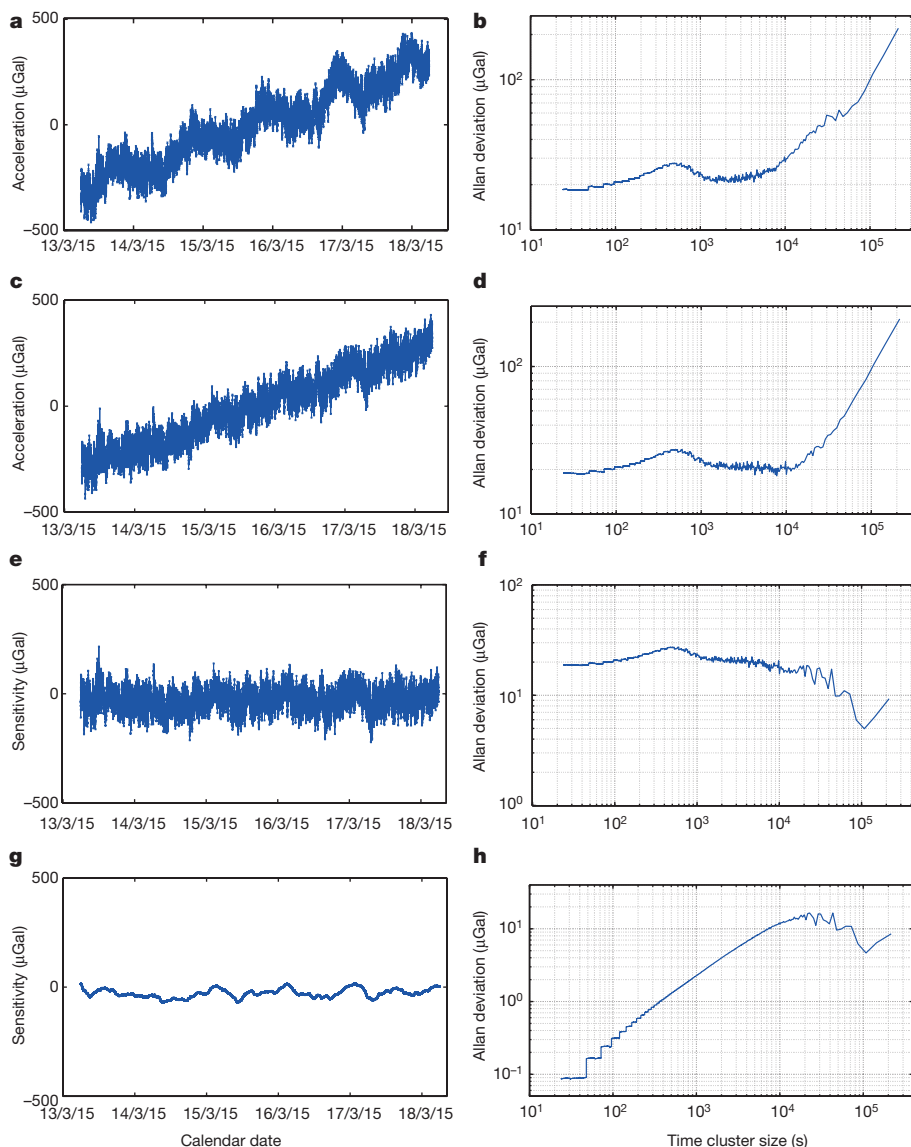
Figure 4 | Drift characteristics. a, A full noise time series of the tide measurement. **b**, The Allan deviation of the series in **a**. **c**, A full noise time series of the tide measurement with the tide signal removed via a regression against the theoretical data from *TSOFT*[19]. **d**, The Allan deviation of the series in **c**. **e**, A time series of the tide measurement with the tides removed and the linear drift corrected. **f**, The Allan deviation of the series in **e**. **g**, The same data as in **e** but with a 240-min filter added. **h**, The Allan deviation plot of the filtered data in **g**.

Fig. 4a, c, e and g respectively. Allan deviation is a technique used to measure the variation over the full frequency range of a signal by averaging over increasingly larger time intervals[26].

The data analysed in Fig. 4 spans a frequency range from 10^{-5} Hz to 0.03 Hz (the sampling frequency of this data set, which was used to remove the effect of seismic noise). A second data set was taken at a faster sampling rate to observe the response of the device from 0.03 Hz up to the resonant frequency of 2.3 Hz. Both data sets can be observed in Extended Data Fig. 6 in the form of a root-mean-square acceleration sensitivity plot. The Allan deviation for the high-frequency series is polluted by the presence of two large signals: the resonant frequency of the device, and the microseismic peak[27,28]. This deviation plot is not a useful measure of the noise of the device and has therefore not been included in Fig. 4. Figure 4a and c demonstrates the linear drift that the device experiences. Figure 4b, d and f also demonstrates a small peak at 500 s that is an artefact of the temperature servo. The broad peak that is only visible on the rising edge of Fig. 4b is the tide signal. A comparison between the drift characteristics of our device and some other commercial gravimeters is displayed in Extended Data Fig. 7 in which an acceleration power spectral density plot is displayed.

Because this MEMS device is capable of measuring the Earth tides, it is not just an accelerometer, but a gravimeter. Made from a single silicon chip the size of a postage stamp, this sensor has the lowest reported resonant frequency of any MEMS accelerometer (2.3 Hz), is within an order of magnitude of the best acceleration sensitivity of any MEMS device ($40\,\mu$Gal Hz$^{-1/2}$), and has the best reported stability of any MEMS device. This prototype will enable the development of density-contrast imaging technology useful in many industrial, defence, civil and environmental applications. It has the potential to be inexpensive, mass-produced and light-weight, opening up new markets. This MEMS gravimeter could be flown in drones by oil and gas exploration companies, reducing the need for dangerous low-altitude aeroplane flights, it could be used to locate subterranean tunnels, and it could be used by building contractors to find underground utilities. Networks of sensors could be operated in areas unsafe for humans, to monitor natural and man-made hazards, for example, on volcanoes or unstable slopes to measure the spatial and temporal resolution of subsurface density changes and improve hazard forecasting[25,29].

Online Content Methods, along with any additional Extended Data display items and Source Data, are available in the online version of the paper; references unique to these sections appear only in the online paper.

1. Van Camp, M. Uncertainty of absolute gravity measurements. *J. Geophys. Res.* **110,** B05406 (2005).
2. Jiang, Z. *et al.* Relative gravity measurement campaign during the 8th international comparison of absolute gravimeters (2009). *Metrologia* **49,** 95–107 (2012).
3. Lederer, M. Accuracy of the relative gravity measurement. *Acta Geodyn. Geomater.* **6,** 383–390 (2009).
4. Goodkind, J. M. The superconducting gravimeter. *Rev. Sci. Instrum.* **70,** 4131–4152 (1999).
5. de Angelis, M. *et al.* Precision gravimetry with atomic sensors. *Meas. Sci. Technol.* **20,** 022001 (2009).
6. Farrell, W. E. Earth tides, ocean tides and tidal loading. *Phil. Trans. R. Soc. A* **274,** 253–259 (1973).
7. D'Alessandro, A. & D'Anna, G. Suitability of low-cost three-axis MEMS accelerometers in strong-motion seismology: tests on the LIS331DLH (iPhone) accelerometer. *Bull. Seismol. Soc. Am.* **103,** 2906–2913 (2013).
8. Krishnamoorthy, U. *et al.* In-plane MEMS-based nano-g accelerometer with sub-wavelength optical resonant sensor. *Sens. Actuat. A.* **145–146,** 283–290 (2008).
9. Lainé, J. & Mougenot, D. A high-sensitivity MEMS-based accelerometer. *Leading Edge* **33,** 1234–1242 (2014).
10. Pike, W. T. *et al.* A self-levelling nano-g silicon seismometer. In *Proc. IEEE Sensors 2014* 1599–1602, http://ieeexplore.ieee.org/xpl/articleDetails.jsp?arnumber=6985324 (IEEE, 2014).
11. Bertolini, A., Cella, G., Desalvo, R. & Sannibale, V. Seismic noise filters, vertical resonance frequency reduction with geometric anti-springs: a feasibility study. *Nucl. Instrum. Meth. A* **435,** 475–483 (1999).
12. Cella, G. *et al.* Seismic attenuation performance of the first prototype of a geometric antispring filter. *Nucl. Instrum. Meth. A* **487,** 652–660 (2002).
13. Pike, W. T., Standley, I. M. & Calcutt, S. A silicon microseismometer for Mars. In *Transducers and Eurosensors XXVII* 622–625, http://ieeexplore.ieee.org/xpl/articleDetails.jsp?arnumber=6626843 (IEEE, 2013).
14. Carbone, L. *et al.* Sensors and actuators for the Advanced LIGO mirror suspensions. *Class. Quantum Gravity* **29,** 115005 (2012).
15. Bell, C. J., Reid, S. & Faller, J. Experimental results for nulling the effective thermal expansion coefficient of fused silica fibres under a static stress. *Class. Quantum Gravity* **31,** 065010 (2014).
16. Watanabe, H., Yamada, N. & Okaji, M. Linear thermal expansion coefficient of silicon from 293 to 1000 K. *Int. J. Thermophys.* **25,** 221–236 (2004).
17. Poggi, M. A., McFarland, A. W., Colton, J. S. & Bottomley, L. A. A method for calculating the spring constant of atomic force microscopy cantilevers with a nonrectangular cross section. *Anal. Chem.* **77,** 1192–1195 (2005).
18. Cho, C. H. Characterization of Young's modulus of silicon versus temperature using a "beam deflection" method with a four-point bending fixture. *Curr. Appl. Phys.* **9,** 538–545 (2009).
19. Van Camp, M. & Vauterin, P. Tsoft: graphical and interactive software for the analysis of time series and Earth tides. *Comput. Geosci.* **31,** 631–640 (2005).
20. Callen, H. B. & Welton, T. A. Irreversibility and generalized noise. *Phys. Rev.* **83,** 34–40 (1951).
21. Chin, E., Lee, K., Winterood, J., Ju, L. & Blair, D. Low frequency vertical geometric anti-spring vibration isolators. *Phys. Lett. A* **336,** 97–105 (2005).
22. Sainz-Maza Aparicio, S., Sampedro, J. A., Montesinos, F. G. & Molist, J. M. Volcanic signatures in time gravity variations during the volcanic unrest on El Hierro (Canary Islands). *J. Geophys. Res.* **119,** 5033–5051 (2014).
23. Mogi, K. Relations between the eruptions of various volcanoes and the deformations of the ground surfaces around them. *Bull. Earthq. Res. Inst.* **36,** 99–134 (1958).
24. Battaglia, M., Gottsmann, J., Carbone, D. & Fernandez, J. 4D volcano gravimetry. *Geophysics* **73,** WA3–WA18 (2008).
25. Rymer, H., Williams-Jones, G. & Keynes, M. Gravity and deformation measurements. *Geophys. Res. Lett.* **27,** 2389–2392 (2000).
26. Allan, D. Statistics of atomic frequency standards. *Proc. IEEE* **54,** 221–230 (1966).
27. Peterson, J. *Observations and modeling of seismic background noise.* US Geological Survey Open-file Report Number 93-322, http://www.mttmllr.com/ADS/DATA/peterson_usgs_seismic_noise_ofr93-322.pdf (USGS, 1993).
28. Essen, H. H., Kruger, F., Dahm, T. & Grevemeyer, I. On the generation of secondary micro-seisms observed in northern and central Europe. *J. Geophys. Res.* **108,** 2506–2520 (2003).
29. Baxter, P. J. & Gresham, A. Deaths and injuries in the eruption of Galeras volcano, Colombia, 14 January 1993. *J. Volcanol. Geotherm. Res.* **77,** 325–338 (1997).

METHODS

MEMS device fabrication. The MEMS device was fabricated from a single chip of 200-μm-thick silicon. The reverse side of the wafer was first coated with 2.5 μm of plasma-enhanced chemical vapour deposition (PECVD) SiO_2. A 100-nm coating of chromium was next deposited on the top surface of the silicon using a thermal evaporator.

The MEMS device pattern was created in a layer of positive photoresist using a g-line photolithography process. The mask was a 'halo' design[31] that is, instead of etching away all of the unwanted areas of silicon, trenches were used in an outline of the structure, to keep a constant etch rate and profile over all etched areas. The halo was 10 μm wide. The photoresist pattern was then used as a mask to wet-etch the chrome using a nitric acid chrome etchant for 100 s, thus etching the MEMS device proof mass pattern into the chrome. The resist was then removed ultrasonically with acetone and isopropanol, leaving the chrome etch mask in place. A 7-μm layer of AZ-4562 photoresist was then spun onto the back of the sample and used later to make the sample free-standing.

The sample was fixed to a carrier wafer (chrome side up) using a thin, spun-on layer of Crystalbond 509 (as mounting adhesive) in solution with acetone. To ensure a good thermal contact the sample was weighted and left on the hotplate at 88 °C (just above the melting point of Crystalbond 509) for 5 min. The sample was next placed in an Oxford Instruments PlasmaPro 100 Estrelas Deep Silicon Etch System, and Bosch-etched[32] for 80 min using an SF_6, C_4F_8 process optimized for highly anisotropic trenches. This etch was the same depth as the silicon and stopped when it reached the SiO_2 back layer. The PlasmaPro 100 Estrelas Deep Silicon Etch System allows control of the gas flow, enabling processes to be tuned with negative and positive defined etch profiles. Our spring profiles are vertical to within 0.5°.

To remove the sample from the carrier wafer it was heated to 88 °C for 5 min, and then pushed laterally off the Crystalbond 509, which is now fluid. The SiO_2 and the AZ–4562 layers enabled this to be done without damaging the MEMS device structure. The sample was then turned upside down and placed (not affixed) on a blank piece of silicon. The residual Crystalbond 509 and photoresist were removed from the bottom of the sample using an O_2 plasma ash. The sample was exposed to a CF_4/O_2 etchant plasma until all of the SiO_2 was removed, making the sample free-standing.

Geometrical anti-spring design. Our MEMS device is comprised of a proof mass suspended from three curved cantilevers/flexures. To better understand the physical characteristics of this system we first discuss these flexures individually. Consider a cantilever, clamped at one end, and free to move at the other. A proof mass mounted on the moving end will oscillate with a frequency that depends on the geometry of the cantilever, and the Young's modulus of the material from which it is made. The proof mass will oscillate along an arc defined by the length of the flexure. The system will behave as a Hooke's law spring, with a linear relationship between force and displacement. This behaviour can be observed in Extended Data Fig. 4a. A curved single cantilever also behaves in the same manner, as seen in Extended Data Fig. 4b.

To create an anti-spring, one can take two such curved cantilevers and attach them at a central pivot point. A proof mass mounted at this point will no longer be able to trace out an arc as it oscillates. Instead, because of the symmetrical forces applied by the two identical cantilevers, its motion will be constrained along a vertical axis (as presented in Fig. 1). It is this constraint that causes the spring constant to change as the displacement increases. Instead of observing a linear relationship between force and displacement, a nonlinear behaviour is observed (see Extended Data Fig. 4c). This now means that the spring gets softer with increasing displacement.

A four-flexure anti-spring system is a simple extension of a two-flexure system. Here, a second pair of cantilevers are placed below the first pair, which allows a non-point-source proof mass to be suspended. The behaviour of the spring is still nonlinear, and is displayed in Extended Data Fig. 4d. The behaviour is identical to that of a two-flexure system, except the system can support twice the mass.

Both the two- and four-flexure anti-spring systems can be used to create oscillators that have low resonant frequencies. When the limits of k/m are pushed to create the lowest resonant frequency possible, however, these systems become unstable. They become unstable because the motion is so well constrained along its vertical axis that the spring gets softer and softer until it can no longer support the weight of the proof mass. This behaviour can be observed in Extended Data Fig. 4c and d: as the force increases, the displacement increases rapidly. A stable resonant frequency is imperative for a useful relative gravimeter, so this instability would create problems if used for the design of a MEMS gravimeter. It would require the use of a closed-loop feedback system.

Our MEMS device utilizes a novel three-flexure anti-spring system, with one flexure of the upper pair of cantilevers removed (see Fig. 1). In the first instance, the device behaves as a four-flexure anti-spring: it gets rapidly softer as the

displacement of the proof mass increases. The anti-spring behaviour is maintained while the proof mass moves along its vertically constrained axis. The asymmetry of the system, however, means that the device does not stay constrained along the anti-spring constraining axis. The single upper flexure ultimately tilts the proof mass marginally away from the constraining axis. As the motion is pulled from this axis, the anti-spring trend is halted and the device regains a Hooke's law behaviour, where $\mathrm{d}F/\mathrm{d}z$ is a constant. This behaviour can be observed in Extended Data Fig. 4e, where the gradient of force versus displacement reaches a minimum at $z = 0.6$. This means that the device assumes a constant value of k at the minimum stiffness value that we have demonstrated to be stable over many months (as demonstrated by Extended Data Fig. 9).

Optical shadow sensor. The proof mass motion is measured using an optical shadow sensor[14]. Using a fused silica 'C'-shaped support structure, a red LED (powered at 0.3 mW) was shone onto a split photodiode, with the MEMS device proof mass mounted in between. The change in intensity incident on the photodiode resulting from the motion of the proof mass shadow was then used as a measure of the motion. The split photodiode was made from two 5 mm by 10 mm planar silicon photodiodes, and wired to give a differential output. A split photodiode was used so that at the nominal position of the proof mass the output signal was zero. This allowed maximal amplification without saturation of the measurement instrumentation. The LED signal was modulated (at a frequency of 107 Hz with a 50:50 duty cycle) to reduce the $1/f$ noise in the output signal. The modulation was carried out by turning the LED on and off with an HP 33120A square-wave signal generator. A precision current-stabilizing resistor (displayed in Fig. 2) maintained the LED drive current; this resistor was heat sunk to the fused silica 'C'-shaped structure. The current output from the photodiode was first converted into a voltage using a Stanford Research Systems SR570 current-to-voltage converter, band-passed between 3 Hz to 100 Hz, and amplified by a factor of $10^6 \, \mathrm{V\,A}^{-1}$. This amplified signal was then de-modulated via an analogue lock-in amplifier (Femto LIA-MV-200) referenced from the signal generator. The lock-in amplified the signal with a gain of ten and undertook readings with a time constant of 3 s. This analogue signal was passed through a Stanford Research Systems SR560 low pass filter of 0.03 Hz, 12 dB per octave, to remove aliasing and filter seismic noise, before being digitized via a 16-bit, analogue-to-digital converter (National Instruments M Series 6229) and recorded by a computer with a 24-s time constant. Analogue signals were used to reduce digitization noise that would have occurred if a digital signal had been amplified by this magnitude.

The shadow sensor has a read-out noise floor of $\leq 10 \, \mu$Gal at the sampling frequency of 0.03 Hz, and a dynamic range of about 50 μm. A large dynamic range is required because of the large initial displacement (0.8 mm) of the proof mass when it is tilted to its vertical operating orientation, thus making initial alignment of the MEMS device difficult. Although the maximum peak-to-peak displacement of the proof mass caused by the tides is only 16 nm, the proof mass also oscillates at its resonant frequency by up to 100 nm owing to seismic ground motion. A high dynamic range is also useful to measure this signal, which is ultimately removed from the data by averaging with a 0.03 Hz filter in the read-out electronics.

Temperature control. The control loops used to maintain the temperature of the system were proportional integral derivative control mechanisms, written in Labview (http://www.ni.com/labview/). Temperatures were monitored using a four-terminal measurement of small platinum resistors, via two Keithley 2000 digital multimeters. A four-terminal measurement eradicates contact resistance by driving the thermometer with a current and measuring the voltage across it. This removes the temperature sensitivity of external wires. Low-temperature-coefficient Manganin alloy wires were used for these connections to minimize parasitic thermal conduction. One platinum resistor was placed on the outer frame of the MEMS device and three were placed equidistantly around the copper shield. Wire wound resistors were used as the heating mechanism to feedback into the system; again, one of these was placed on the MEMS device frame and three around the shield. The output signal to the heaters was sent via a National Instruments (USB 6211) digital-to-analogue converter (DAC) card, and the heaters were powered with non-inverting amplifiers with a capability to power up to 100 mA. All circuitry and instrumentation used to amplify and measure the output signal, and to measure and control the system temperature, were selected for their high thermal stability. This entire configuration was constructed in a vacuum chamber with a pressure of $\leq 10^{-5}$ mTorr.

Data analysis. Although proportional integral derivative (PID) temperature control was implemented for the MEMS device and the shield, there were other components with variations that could not be actively controlled. These were the room temperature that coupled into the data via a temperature-sensitive lock-in amplifier, and the intensity variations of the LED, which were monitored using a monitor photodiode. There was also an offset, and a linear drift of under 150 μGal per day once the system had been left evacuated for over a week. This drift term is due to stress in the silicon flexures. Like all mechanical systems, application of stress leads to

anelasticity, which causes creep and drift over long timescales. Our device also shows polynomial drift which decays away approximately one week after evacuating the apparatus. The polynomial drift is probably due to adsorbed water on the surface layer of silicon, and could be mitigated by baking out the system before evacuation. Extended Data Fig. 5 demonstrates this initial polynomial drift. The data were therefore regressed against the temperature measurements listed above, the drift offset and the intensity. This regression—carried out in Matlab (http://uk.mathworks.com/products/matlab/) with the *mregg* tool—identified correlations between the output data and these parameters, and removed any resulting correlated trends from the final data. Floor tilt and power variation of the LED were also monitored, but neither had any discernible effect on the signal and were therefore not regressed.

The correlation coefficient, R, between the averaged theoretical and experimental tide data was calculated using Matlab's *corrcoeff* function. An R value of 0.86 was produced for the plot presented in Fig. 3. To check the level of statistical significance of our experimental data we compared it to the correlation of the noise alone. We created 10,000 random permutations of our data set and calculated the correlation coefficient for each with respect to the theoretical data. This set of R values was plotted as a histogram. This histogram had a distribution with a mean value of zero and a standard deviation of 0.008. The R value from the un-randomized data are 114σ from this distribution, suggesting the correlation is real to an extremely high degree of confidence.

Extended Data Fig. 6 is a plot of the root-mean-square acceleration sensitivity of the device over its full spectral range. The tide signal can be observed at 1×10^{-5} Hz. The peak at 10^{-3} Hz is an artefact of the temperature servo. Between 0.1 Hz and 0.2 Hz the microseismic peak can be recognized; its presence indicates that the device is also a sensitive seismometer. Past observations—made in Scotland from February to March 2000—of the microseismic peak[28] confirm the validity of our observation. At 2.3 Hz the primary resonant mode of the MEMS device generates a large peak due to excitation from seismic noise. This plot was used to calculate the sensitivity of the MEMS device. To find a sensitivity in microgal per hertz[1/2], it is only necessary to read off the acceleration sensitivity at the point where the data crosses 1 Hz on the horizontal axis. We believe that the value of $40\,\mu\mathrm{Gal\,Hz}^{-1/2}$ is an overestimate of the true sensitivity of the device because at 1 Hz the influence of both the primary resonance of the device and the micro-seismic peak are important.

Tilt variation. Although tilt did not have an effect on the tide measurement, we are interested to know at what point tilt would become an issue. Extended Data Fig. 8 presents two plots of an experiment used to assess the effect of tilt on our device. Inside the vacuum tank, the MEMS device was mounted vertically and aligned with the tilt sensor. The y axis of the tilt sensor was aligned with the plane of the MEMS device, with the x axis perpendicular to this (see Fig. 1). Extended Data Fig. 8a demonstrates the induced tilt of the tank and the output of the MEMS device along the x axis. Extended Data Fig. 8b shows the same data as in Extended Data Fig. 8a, but for the y axis. There is a strong correlation between the y-axis variation and the voltage output, giving a tilt sensitivity in this axis of $21.2\,\mu\mathrm{Gal}$ per arcsecond. There is less sensitivity to the x-axis tilt with a tilt sensitivity of only $0.6\,\mu\mathrm{Gal}$ per arcsecond.

The x-axis tilt sensitivity is low because in the vertical configuration the spring resumes a Hooke's law response, as observed in Extended Data Fig. 1, for which the x-axis tilt variation is plotted against the resonant frequency (the acceleration sensitivity of the device is proportional to the square of the resonant frequency). Ultimately the spring could be tuned to operate with even less variation with tilt in this axis if it were positioned to operate at one of its minima. Alternatively the flexures could be made marginally thicker to shift the minimum in resonant frequency to 90°; this was not carried out because the device did not show sufficient tilt sensitivity to cause concern. The y-axis variation is larger because the device has a mode of oscillation in which the proof mass tilts and pivots about the upper cantilever flexure.

When vertical, the device would need to be levelled with an accuracy limited by the y-axis sensitivity (that is, less than 2 arcsec to maintain the current sensitivity) to make repeatable measurements in different locations. This accuracy of levelling is achievable with a simple surveyor's bubble level.

Temporal reproducibility tests. Extended Data Fig. 9 demonstrates two short data sets separated by nearly four months. These were used as a test of the temporal stability of the device. To convert the raw voltage output of the device into a unit of acceleration, a calibration factor was required. By comparing the experimental (blue line) data in Extended Data Fig. 9a with that in Extended Data Fig. 9b we were able to test whether the calibration factor had drifted over time. The same calibration factor has been used to make both of these plots. By averaging the data and changing the calibration factor of Extended Data Fig. 9b, it was found that a change in the calibration factor of 5% made the fit to the tide theory (red line) data noticeably worse. Changes smaller than this were not resolvable. We therefore believe that if the calibration factor has changed, it has done so by no more than 5%. During this period, the vacuum tank was vented and evacuated several times, and the MEMS was moved around each time. This is an important feature of a device that could eventually be used in the field.

Applications. MEMS gravimeters have many industrial applications. Given their small size and low cost, they could be used for down-borehole exploration in the oil and gas industry[33] and used to monitor well drainage. Such devices could also be used for environmental monitoring, where networks of sensor arrays could monitor subsurface water levels[34], or to determine the location of historic landfill sites. In the security industry, low-cost and small-size gravimeters would also be useful in detecting subterranean tunnels[35,36] or for imaging of cargo containers, where high spatial resolution via numerous sensors is an advantage[37]. MEMS gravimeters could also be used in civil engineering. For example, at present in the UK, for many cities built in the Victorian period the placement of utilities is accurate on maps only to within 15 m of landmarks such as trees, fences or buildings. There have been trials of the Scintrex CG5 and MEMS-based arrays should improve mapping resolution. Gravimetry is already used in volcanology and could help to predict eruptions using networks of small, low-cost gravimeter arrays[22,24,25].

A field prototype is currently being developed in Glasgow that will be the size of a tennis ball and require a power supply of under 1 W. A powerless getter pump will be used to maintain vacuum, both the thermal control and the optical read-out will be on-chip; tilt levelling will be included, and all of the read-out and control software will be run on a micro-controller.

30. Riccardi, U., Rosat, S. & Hinderer, J. Comparison of the Micro-g LaCoste gPhone-054 spring gravimeter and the GWR-C026 superconducting gravimeter in Strasbourg (France) using a 300-day time series. *Metrologia* **48,** 28–39 (2011).
31. Pike, W. Analysis of sidewall quality in through-wafer deep reactive-ion etching. *Microelectron. Eng.* **73–74,** 340–345 (2004).
32. Laermer, F. & Schilp, A. Method of anisotropic etching of silicon. US patent number 5,501,893 (1996).
33. Rim, H. & Li, Y. Advantages of borehole vector gravity in density imaging. *Geophysics* **80,** G1–G13 (2015).
34. Bauer-gottwein, P., Christiansen, L. & Rosbjerg, D. Informing hydrological models with ground-based time-lapse relative gravimetry: potential and limitations. In *Proc. Symp. J-H01 (GRACE, Remote Sensing and Ground-based Methods in Multi-Scale Hydrology)* 187–194 (IAHS Publ. 343, 2011).
35. Romaides, A. J. *et al.* A comparison of gravimetric techniques for measuring subsurface void signals. *J. Phys. D* **34,** 433–443 (2001).
36. Butler, D. K. Microgravimetric and gravity gradient techniques for detection of subsurface cavities. *Geophysics* **49,** 1084–1096 (1984).
37. Kirkendall, B., Li, Y. & Oldenburg, D. Imaging cargo containers using gravity gradiometry. *IEEE Trans. Geosci. Remote Sens.* **45,** 1786–1797 (2007).
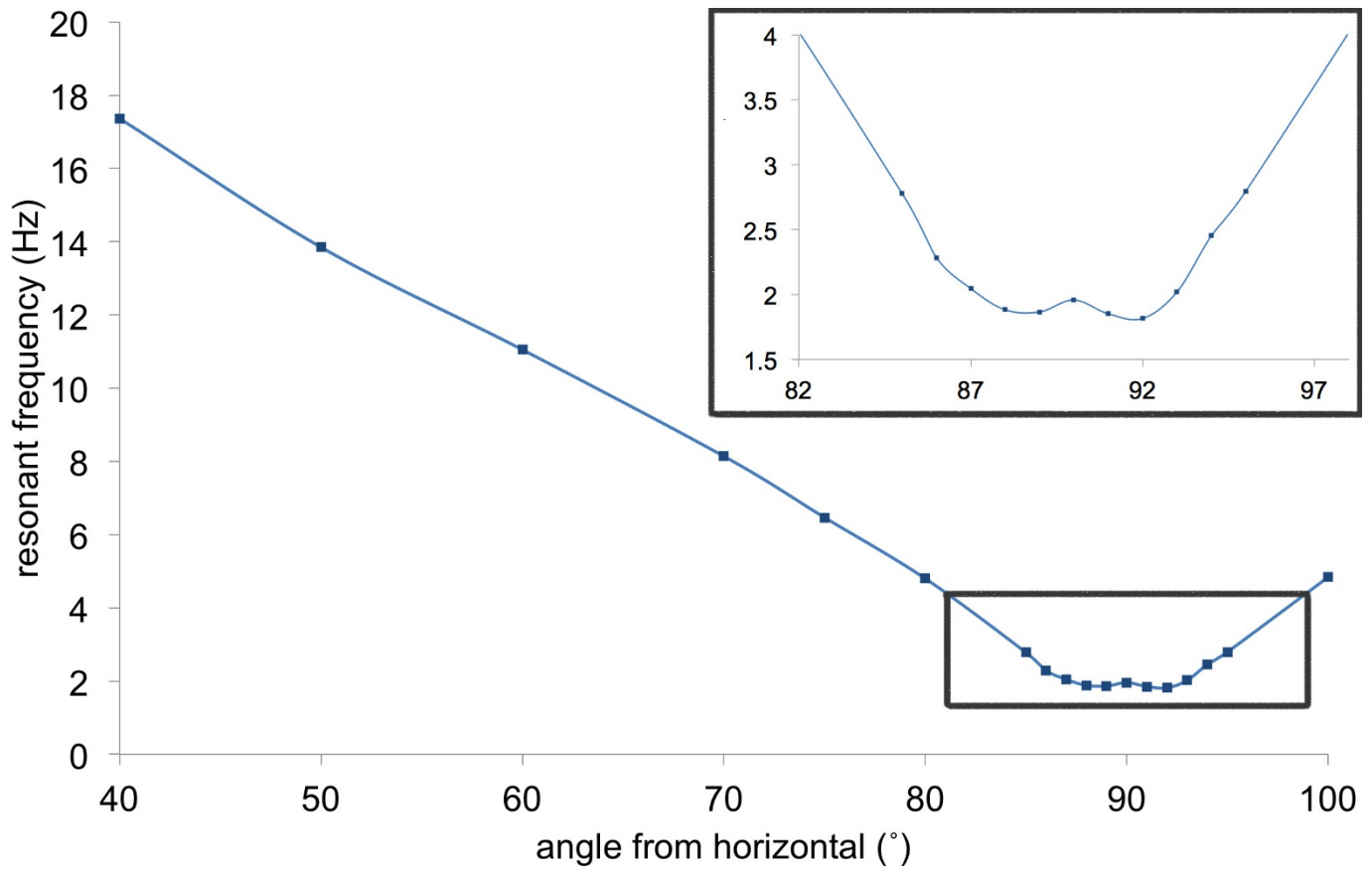
Extended Data Figure 1 | Spring resonant frequency behaviour with tilt. The resonant frequency decreases as the MEMS device gets closer to vertical due to the geometrical anti-spring effect. At 88° and 92° there are minima in the plot (see inset). At this point the frequency is constant with tilt and the system displays Hooke's law behaviour. The resonant frequency of a symmetric anti-spring would reach an instability here. This figure also demonstrates that while the instrument is operated at 90° the resonant frequency is 2.3 Hz. It can be lowered to 1.8–1.9 Hz by tilting to operate at one of the minima.

(a)

(b)
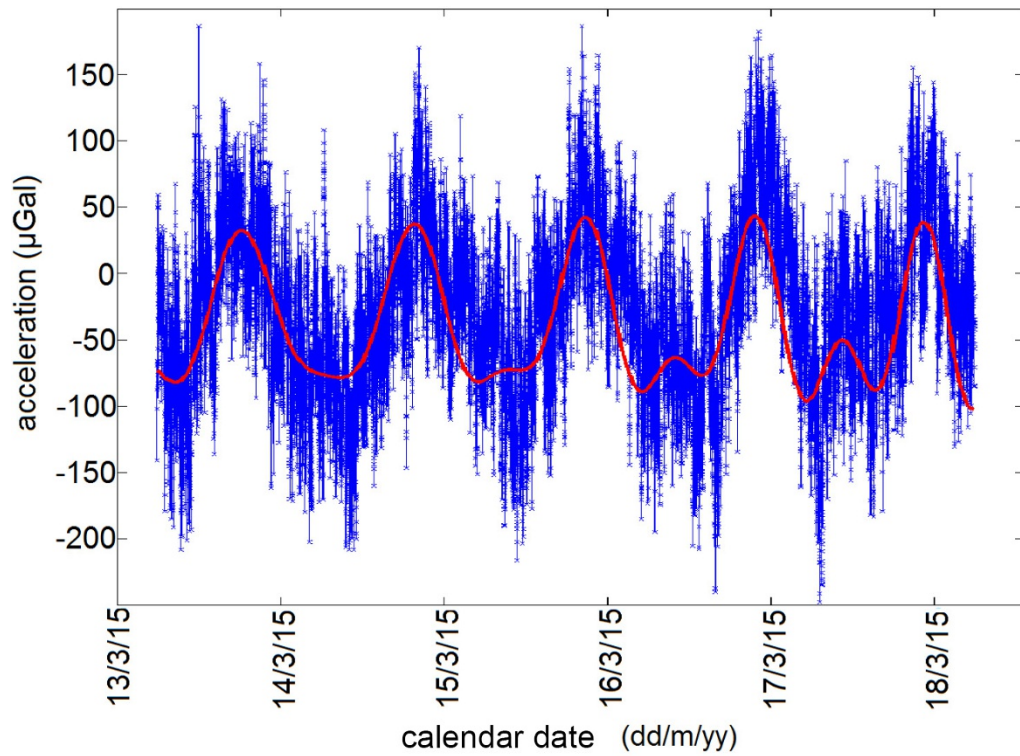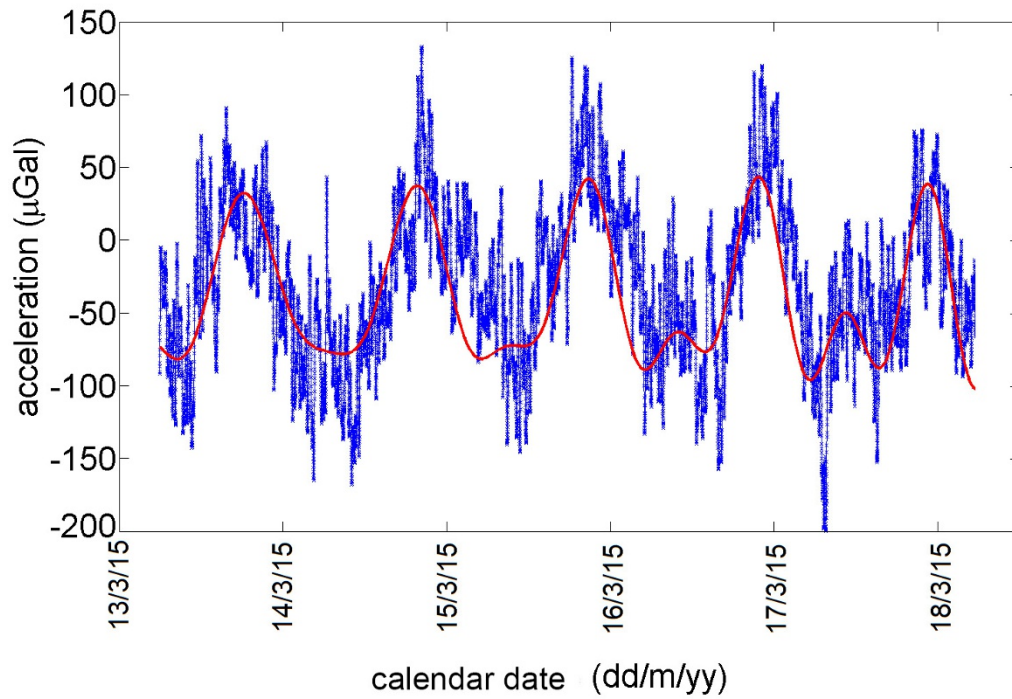
Extended Data Figure 2 | The Earth tides with different filtering. a, Measurements of the Earth tides obtained from the MEMS device. This is the raw data output. **b**, The same data but with a 10-min filtering time. The red lines are theoretical plots calculated by *TSOFT*. The blue lines are the experimental data.
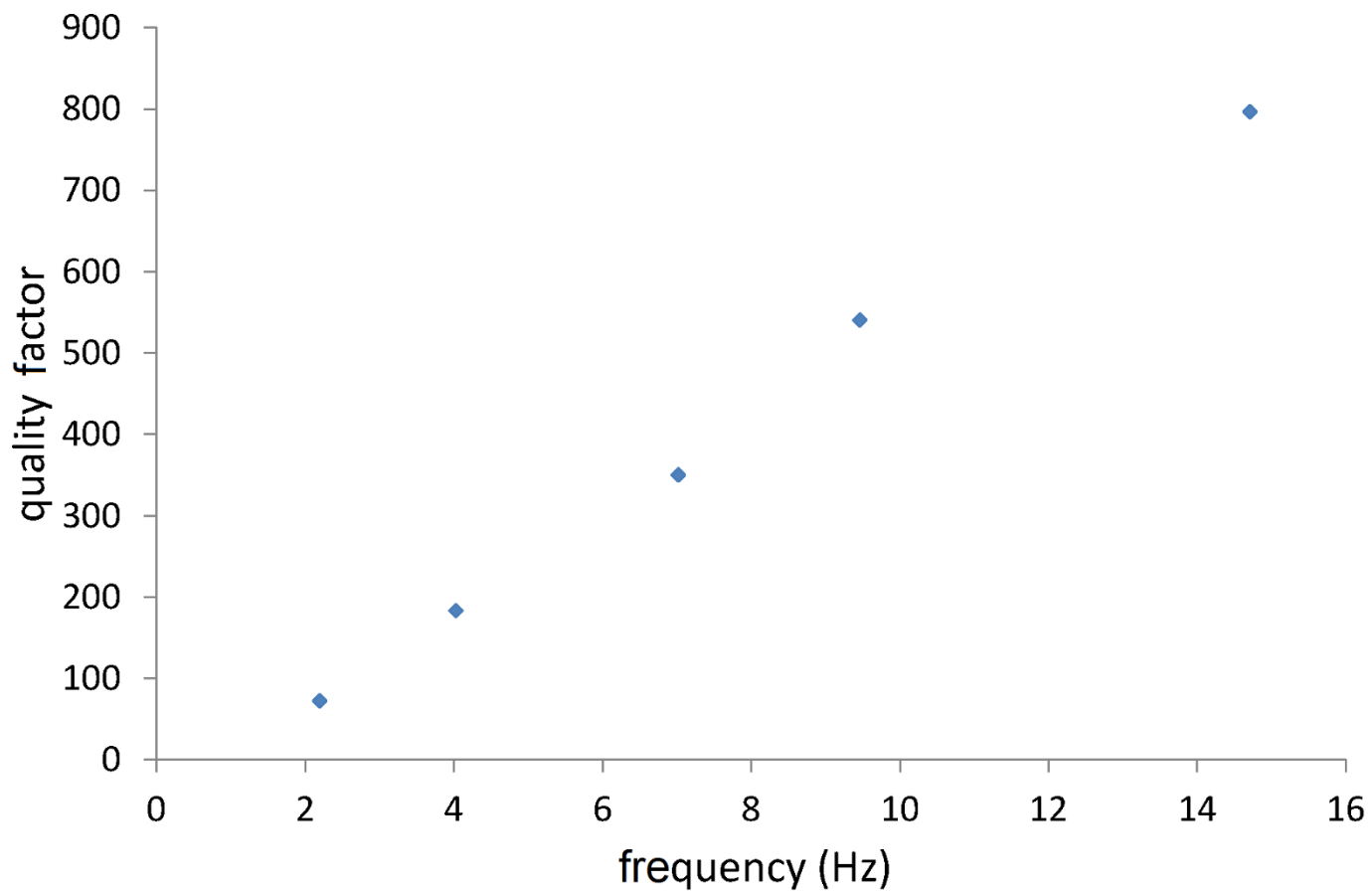
Extended Data Figure 3 | Quality factor frequency dependence. We observe a trend of decreasing quality factor with decreasing frequency of our device. At low frequencies the internal friction of the material becomes the dominant loss mechanism. This trend has been discussed by ref. 21.
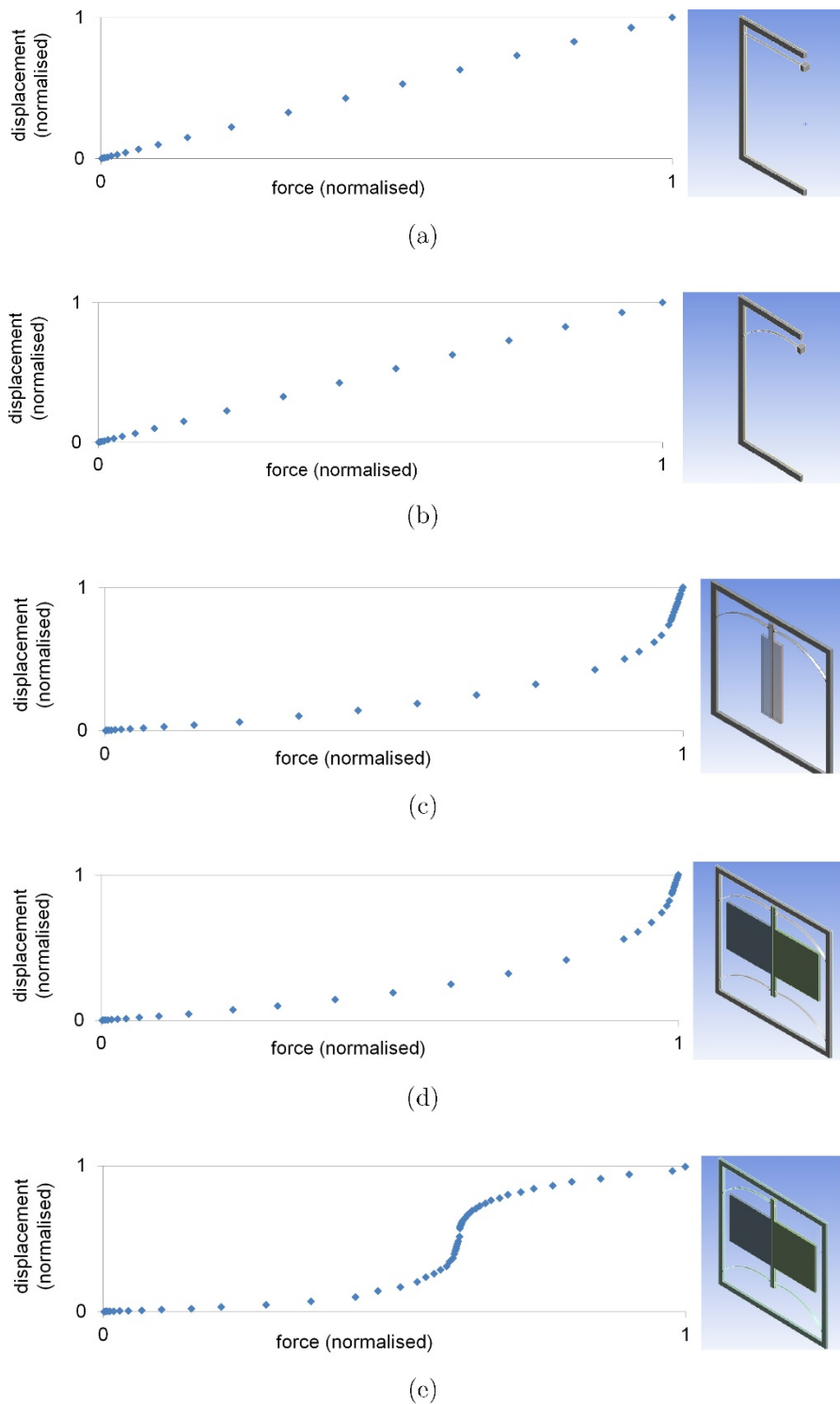
Extended Data Figure 4 | Geometrical anti-spring design. a and **b** demonstrate the Hooke's law behaviour of a straight and curved cantilever, respectively. **c** and **d** demonstrate the unstable anti-spring characteristics of a 2- and 4-flexure MEMS device, respectively. **e**, The behaviour of a 3-flexure MEMS device (see Fig. 1). Whereas a 2- or 4-flexure system reaches an instability with increasing load, a 3-flexure system regains Hooke's law behaviour. The 3-flexure system behaves as such because it is pushed off its constrained axis by the asymmetry of the design. All of these plots were produced using Ansys finite element analysis software (http://www.ansys.com/en-GB).
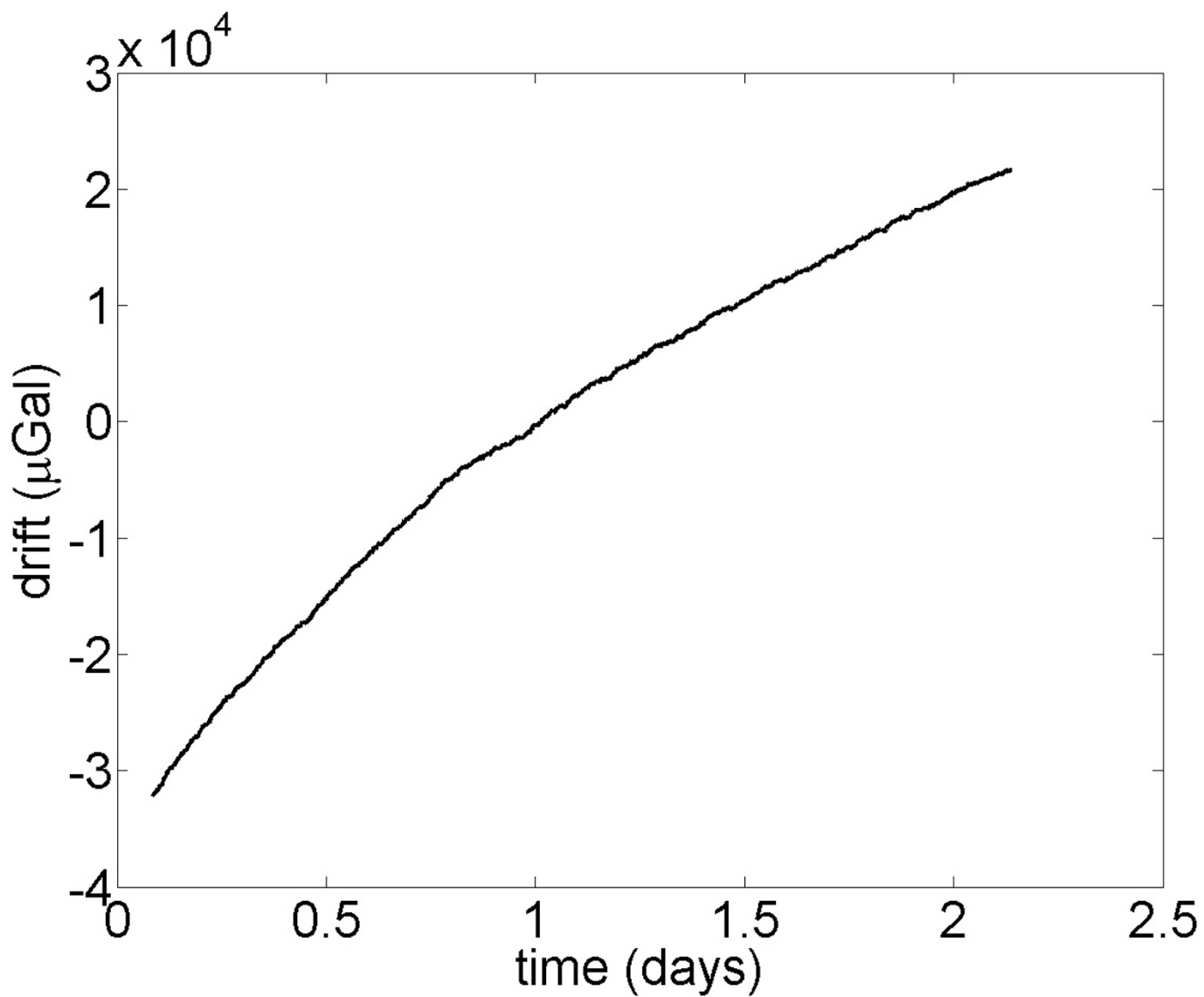
Extended Data Figure 5 | Polynomial drift. This plot demonstrates the drift in the data shortly after the vacuum pump has been turned on. A polynomial component to the drift is clearly visible. Once the vacuum system has settled, however, the drift becomes linear, as demonstrated in Fig. 4b, at a level of $150\,\mu$Gal per day.

(a)

(b)
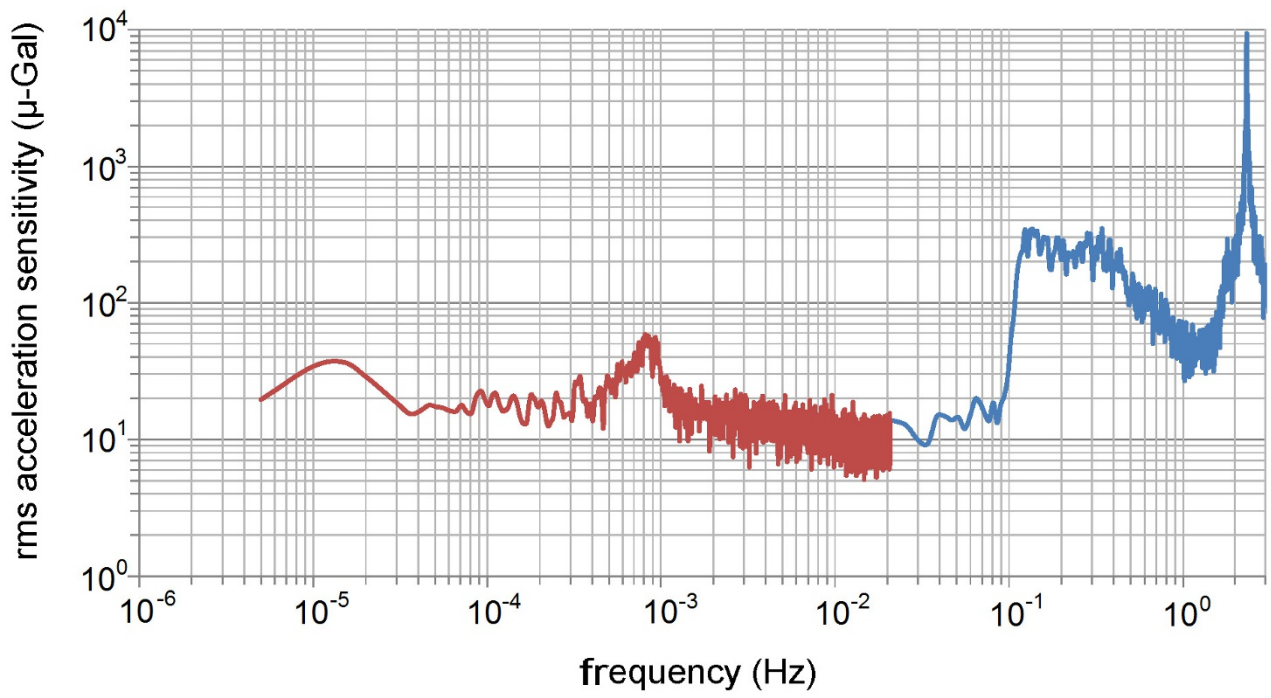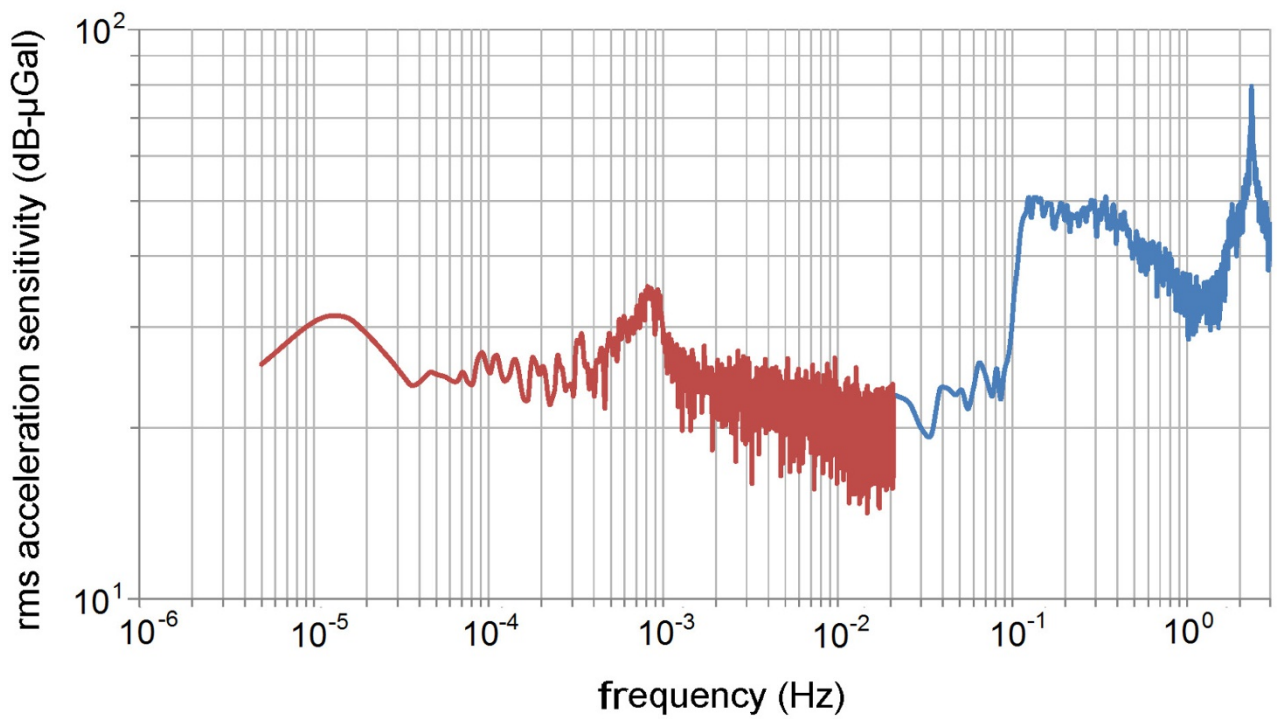
Extended Data Figure 6 | MEMS device root-mean-square acceleration sensitivity. a, The root-mean-square acceleration sensitivity in microgal. **b**, The root-mean-square acceleration sensitivity in decibel microgal. The tide signal can be observed in both plots at 10^{-5} Hz; the peak at 2×10^{-3} Hz is the artefact of the temperature servo discussed earlier; the microseismic peak can be observed between 0.1 Hz and 0.2 Hz; and the 2.3-Hz resonant frequency can be observed to the right of the plot (the blue spike at just above 1 Hz). Two different sampling rates were used to capture this data. The blue series was captured at a sampling rate of 70 Hz while the red series was captured at a sampling rate of 0.05 Hz. This was done to minimize the size of the data file.
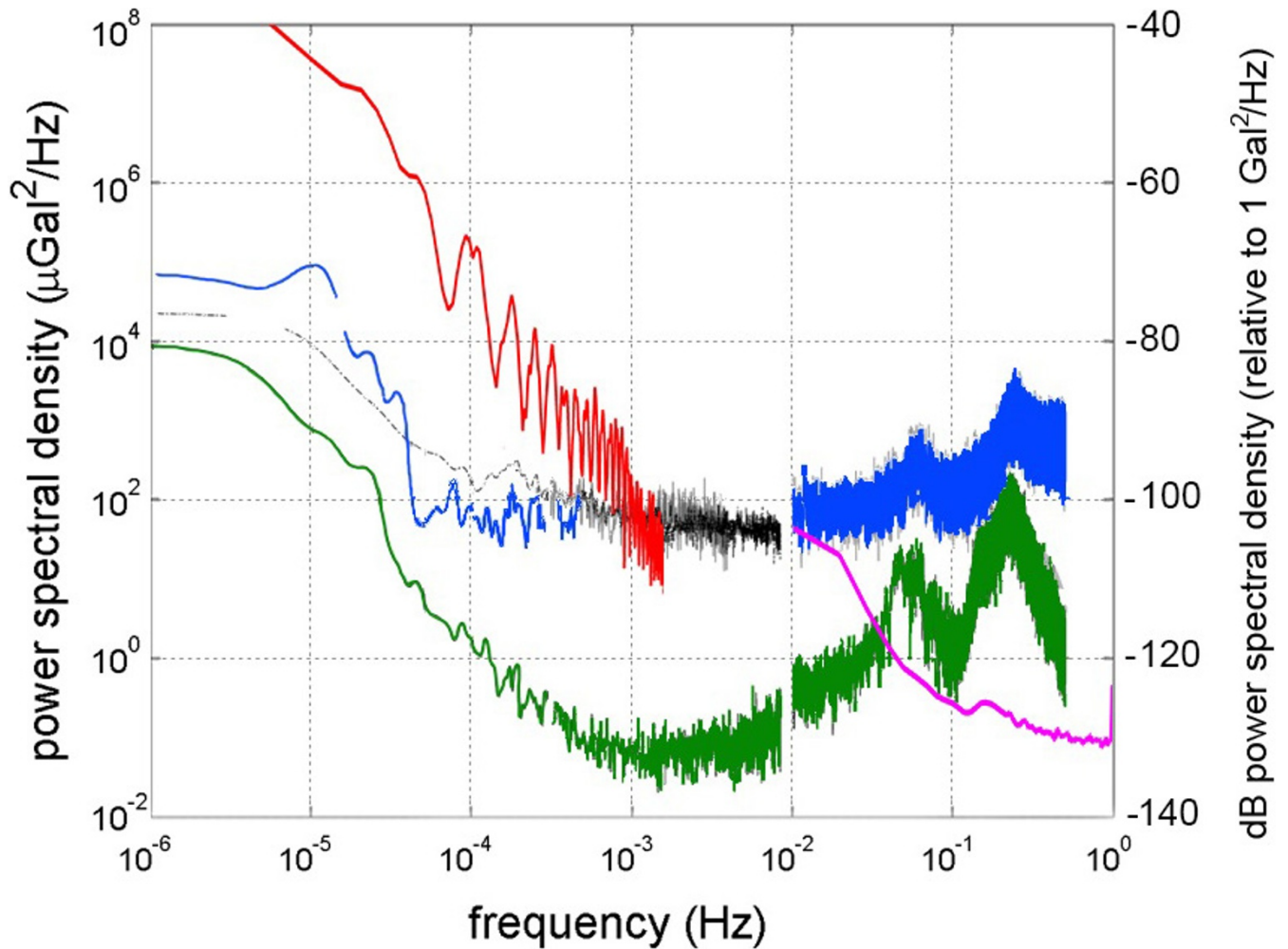
Extended Data Figure 7 | Power spectral density comparison. The red line—plotted using the data from Fig. 4g—represents our MEMS device, demonstrating its sensitivity in the tidal frequency range. The filtering time means that the sensitivity rolls off above 10^{-4} Hz. The black line represents the Scintrex CG5, the blue line the Micro-g Lacoste gPhone-054, the green line the SG-C026 superconducting gravimeter.

The data from these three series are taken from figure 8 in ref. 30 (copyright Bureau International des Poids et Mesures, reproduced by permission of IOP Publishing, all rights reserved). The magenta series represents the microseismometer by W. T. Pike *et al.* (private communication by permission of the author, to be published in the 47th Lunar and Planetary Science Conference).

(a)

(b)
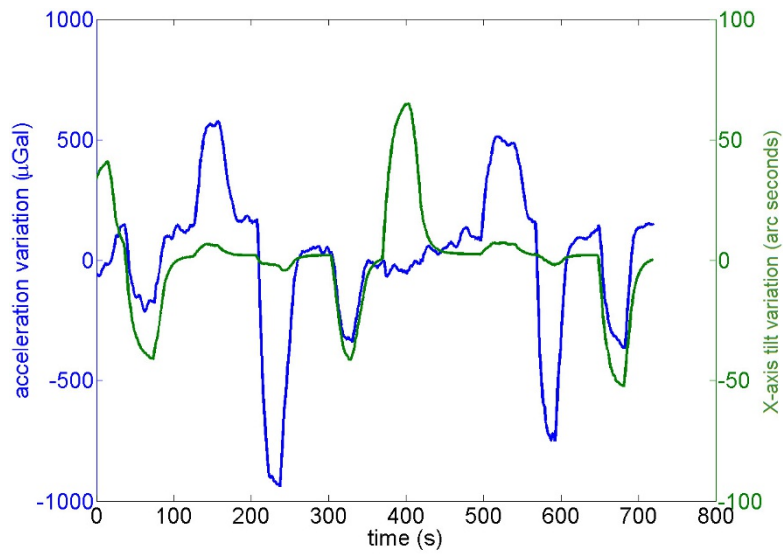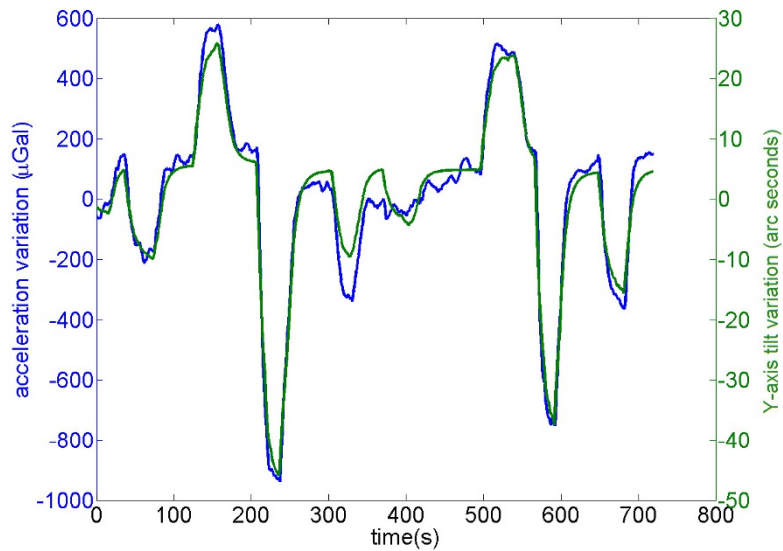
Extended Data Figure 8 | Tilt susceptibility tests. a, The variation in output of the MEMS device with the *x*-axis tilt of the sensor plotted on a secondary axis. **b**, The same as **a** but for the *y* axis. There is an *y*-axis (in-plane MEMS tilt) tilt sensitivity in this axis of 21.2 μGal per arcsecond, but in the *x* axis (out-of-plane MEMS tilt) the tilt sensitivity is only 0.6 μGal per arcsecond.

(a)

(b)
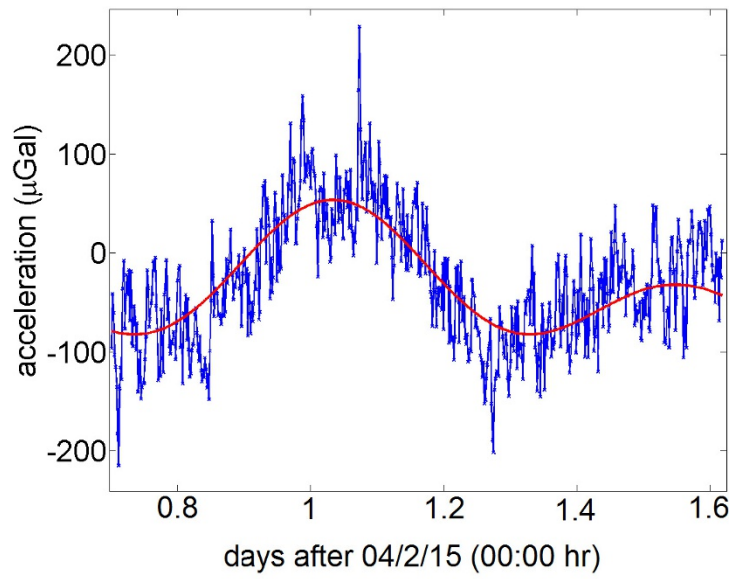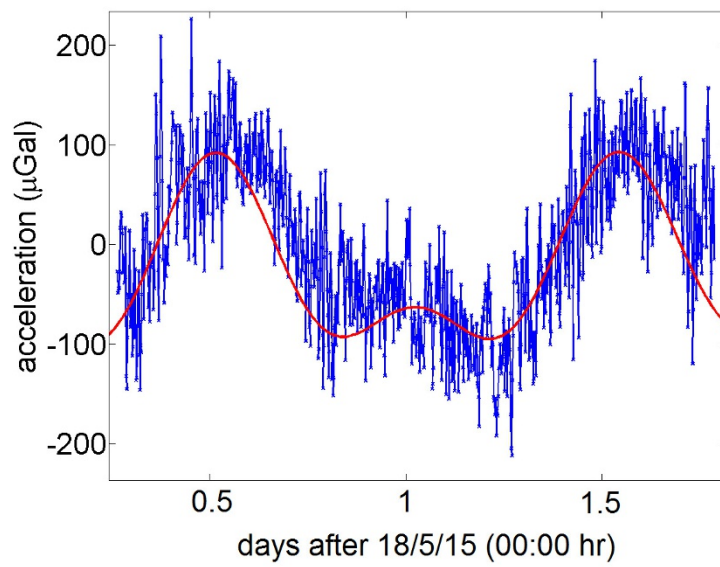
Extended Data Figure 9 | Long-term reproducibility tests. a and **b** are two data sets separated by approximately 4 months, with no filtering employed. During this period the vacuum chamber was evacuated and vented several times, but despite this the calibration factor of the device has not changed by more than 5%.

Extended Data Table 1 | Technology comparison table

Device	Technology	Technology	Stability in the µHz Regime	Resonant Frequency	Use
Scintrex CG5[2,3]	Fused Quartz	2 µGal	0.5 mGal/day	3 Hz	Gravimetry
Krishnamoorthy[8]	MEMS	17 µGal	N/A	36 Hz	Seismology
Quietseis[9]	MEMS	15 µGal	N/A	800 Hz	Seismology
Pike[10]	MEMS	2 µGal	N/A	11 Hz	Seismology
Glasgow MEMS	MEMS	40 µGal	0.14 mGal/day	2.31 Hz	Gravimetry

This table compares the key parameters of several acceleration sensors: the Scintrex CG5[2,3], the Krishnamoorthy[8] MEMS device, the Quietseis[9] MEMS device, the Pike[10] MEMS device, and our own MEMS device.